Rotor performance, blade loads and wake resolution in Navier-Stokes CFD of tidal stream turbines

F. Attene, F. Balduzzi, A. Bianchini, and M. S. Campobasso

Abstract—Reliably predicting turbine/wake interactions in arrays of tidal stream turbines is paramount to reducing losses of energy yield by optimizing array layout at the design stage. This study focuses on the analysis of turbine performance and rotor wakes based on Navier-Stokes computational fluid dynamics, discussing modeling aspects associated with the method used for incorporating turbine hydrodynamics and turbulent flow effects in simulations. Important factors considered herein are a) the impact of laminar-to-turbulent transition of the blade boundary layers on rotor performance, and b) the sensitivity of the computed wake evolution on the turbine modeling approach. For these analyses, the results of rotor resolved and generalized actuator disk solutions are compared to flume tank measured data of a model turbine performance and wake. The overall agreement of all computed solutions and measured data is good. In the presented Reynolds-averaged Navier-Stokes analyses, the rotor-resolved analysis predicts the measured rotor wake up to about four rotor diameters behind the turbine well, and seemingly better than the actuator disk model, as expected; thereafter, however, the rotor resolved simulation dissipates the wake more slowly than observed in the experiment, whereas the wake recovery rate predicted by the actuator disk analysis is closer to measured data. The cross-comparison of the geometry resolved analyses and measured data indicate that the blade boundary layers are likely to be fully turbulent, which has a significant detrimental impact on the turbine power. It is also found that the time-averaged solution of the time-dependent analysis and that of the steady flow analysis of the turbine resolved flow field, differ negligibly, as noted in other recent studies.

Index Terms—Blade load analysis, measured and computed turbine performance and wake characteristics, Navier-Stokes computational fluid dynamics, tidal current turbines, transition modeling.

I. INTRODUCTION

R ENEWABLE energy systems for electrical power generation are rapidly progressing and becoming economically viable, thus contributing to the international commitment to decarbonize this energy sector. The levelized cost of energy (LCOE) of onshore wind is already lower than that of fossil fuel electricity

F. Attene is with the Department of Engineering, Lancaster University, Gillow Avenue, lancaster LA1 4YR, United Kingdom (e-mail: f.attene@lancaster.ac.uk).

F. Balduzzi is with the Department of Industrial Engineering, Universita' degli Studi di Firenze, Via di Santa Marta 3, Firenze 50139, Italy (e-mail: francesco.balduzzi@unifi.it).

A. Bianchini is with the Department of Industrial Engineering, Universita' degli Studi di Firenze, Via di Santa Marta 3, Firenze 50139, Italy (e-mail: alessandro.bianchini@unifi.it).

M.S. Campobasso is with the Department of Engineering, Lancaster University, Gillow Avenue, Lancaster LA1 4YR, United Kingdom (e-mail: m.s.campobasso@lancaster.ac.uk).

generation, and recent year cost surveys indicate that offshore wind LCOE may become competitive with fossil fuel electricity in the next few years [1]. Ocean energy, on the other hand, remains largely unexploited in the UK and other world areas where this resource is particularly abundant. Tidal stream energy (TSE) is a particularly attractive form of ocean energy for electricity generation because it is predictable, it is expected to have a relatively low environmental impact [2], and it does not have significant impact on the seascape. Despite these benefits, the exploitation of TSE is still scarce. This is because of its still high LCOE, caused primarily by high infrastructure, installation and maintenance costs [3]. Moreover, the large-scale exploitation of TSE will also pose scientific and technical challenges resulting from operating a large number of devices in relatively packed arrays, as discussed below.

TSE can be harvested with tidal stream turbines (TSTs), which are often horizontal axis turbines similar to utility-scale wind turbines, installed on the seabed [4]. Due to cost-, bathymetry- and current parameter-related factors, TSTs will operate in large arrays [5], and interactions between wakes shed by upstream turbines and downstream rotors may be unavoidable, resulting in significant reductions of the array energy yield and, in turn, higher LCOE. Therefore, assessing these losses at the array design stage is paramount, and requires methods capable of predicting with sufficient reliability both wake velocity deficit and turbulence characteristics (i.e. intensity and length scales), and rotor performance and its dependence on the turbulence in the oncoming flow. The comparative assessment of several simulation-based approaches to predict TST performance and wake characteristics is the focal point of this article.

Experimental testing, such as one- and multi-turbine flume tank experiments [6]–[8] plays a vital role in both providing reliable turbine and turbulence-dependent wake data to validate all simulation-based tools used for analysis and design of TSTs and arrays at scale, and generating or consolidating knowledge of TST and array hydrodynamics. For example, the experimental analyses in [6] and [7] highlight and quantify the sensitivity of TST wake recovery rates to the ambient turbulence level, and the reduction of TST power with increasing levels of ambient turbulence. A reduction of this kind is also found in the experimental analyses of [9], which also shows that the TST mean power and thrust increase with the turbulence integral length scale.

On the simulation side, several studies using Navier-Stokes Computational Fluid Dynamics (CFD), with varying fidelity level for resolving turbulence and/or modeling its effects on the mean flow field, and varying geometric complexity to account for the flow perturbation due to the presence of TSTs, exist. Available routes to turbulent flow analysis include a) the Reynolds-averaged Navier-Stokes (RANS) approach, whereby the governing equations are time-averaged and turbulent flow effects are accounted for by the Reynolds stresses, b) computationally more costly large eddy simulation (LES) [10], whereby after being grid-filtered the equations are used to directly resolve all turbulence scales supported by the grid, and the sub-grid scale turbulence is dealt with a RANS-like approach, and c) hybrid RANS/LES approaches, such as detached eddy simulation (DES) [11] and delayed DES (DDES) [12], whereby RANS is used in wall regions to reduce mesh requirements and computational costs, and LES is used in the rest of the domain. The key advantage of LES and hybrid RANS/LES over RANS methods is their potential of more accurately resolving the high level of anisotropy of the Reynolds stresses in TST wakes [8], [13].

Options to account for the momentum extraction and wake generation of TSTs include a) the actuator disk (AD) method, whereby the turbine energy extraction is accomplished by a uniform momentum sink [14] or a blade element momentum theory (BEMT) turbine model [15] in the CFD analysis, and the flow field behind the turbine is axisymmetric, b) the actuator line (AL) model [16]–[18], whereby the turbine blades are modeled as rotating lifting lines in the CFD simulation, and c) incorporation of the geometrically resolved blade [19] or entire turbine [20] in the CFD analysis. Both AD and AL models rely on the availability of reliable lift and drag data of the airfoils making up the TST rotor blades. These models use semi-empirical corrections, such as Prandtl tip loss factor, to model the effects of tip and root flows and all other 3D flow physics. The geometry-resolved approach is more general, in that it does not require a-priori knowledge of hydrofoil force data, but its computational cost, particularly when using higher-fidelity approaches to turbulence, is large.

Various combinations of turbine representation and turbulence handling have been considered. Leroux et al. [21] performed turbine geometry-resolved RANS simulations of the one-turbine experiment of [6] at ambient turbulence intensity (TI) of 3%. The turbine design regime they analyzed was characterized by a chord- and relative velocity-based Reynolds number of about 1.4×10^5. Good agreement of measured and computed rotor thrust was found, whereas some discrepancies of measured and computed rotor power were noted. The comparison of measured and computed transverse profiles of wake velocity deficit showed an overprediction of this deficit, fairly independent of the axial position behind the turbine and of whether using a steady (frozen rotor) or a time-dependent (sliding mesh) analysis. The AL and uniform AD models were used in RANS mode by [17] and validated against the

data of [6] and [7]. The study showed good agreement of both methods' predictions of measured wake data for both the isolated rotor wake, and the wake of a rotor operating in the wake of the upstream turbine. The AL predictions were found to agree better than the AD predictions with measured wake data close to the turbine, as expected. The hydrofoil force data for the AL analyses were computed for a range of chord- and relative velocity-based Reynolds number between 10^5 and 10^6, and turbulence length scale of about 10% the rotor diameter. Attene et al. [22] carried out comprehensive validation studies of the RANS/AD method for predicting isolated TST performance and wake, and tidal array wake/turbine interactions and overall power. Overall good agreement between simulations and the considered experimental data [6], [7], [23] was reported, in terms of both turbine performance and wake predictions, but the computed velocity deficit of the wake of a turbine operating in the wake of an upstream turbine differed from measured data more than the computed deficit of the wake of the upstream turbine did.

Geometry-resolved TST CFD analyses were used by Ebdon et al. [24], [25]. Both RANS and DES simulations of a model TST were performed in [24] to assess the wake recovery rate of a TST tested at ambient TI of 1.75% and with turbulence length scale of 1 and 2 rotor diameters. Very good overall agreement of measured and DES wake data were obtained; however, the measured turbine power appeared to be somewhat overpredicted by both DES and RANS analyses. The same group used DDES to analyze the wake data measured in a comprehensive campaign of TST flume tank experiments conducted, varying the inflow TI and turbulent length scale [25]. Overall good agreement of measured and computed wake data was obtained, which tended to worsen only at the highest TI levels. The study also concluded that the wake recovery rate had a strong sensitivity to the level of ambient TI and far less sensitivity to the turbulence length scale, which varied between 0.25 and 1 rotor diameters.

The review above highlights outstanding challenges in TST and tidal array CFD, such as choice of most suitable trade-offs of simulation fidelity and computational costs and uncertainty on hydrofoil force data in surrogate turbine models. The key objectives of the present study are to 1) present and discuss experimentally validated cross-comparative RANS TST analyses using the AD and the geometry-resolved methods, and 2) discuss the choice of the turbine resolution model in light of laminar-to-turbulent transition of the blade boundary layers (BLs) and the assessment of rotor loads.

II. TEST CASE

The test case considered in this study is the model TST tested in the IFREMER flume tank [6]. The flume tank working section has length of 18 m, and rectangular cross test section of width W=4 m. In this experiment, the water depth H is 2 m. The streamwise flow velocity can range from 0.1 to 2.2 m/s. Different levels
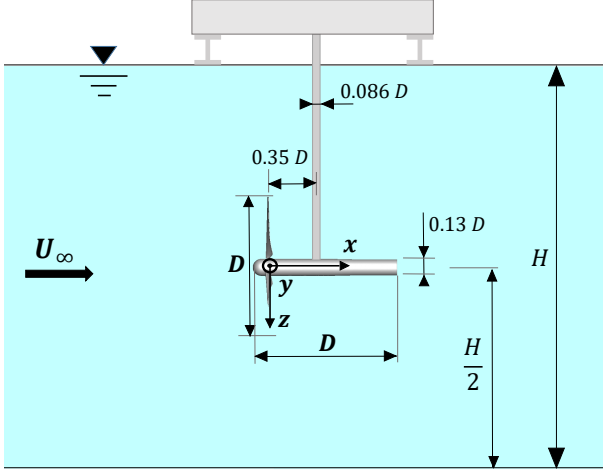
Fig. 1. Side view and key dimensions of IFREMER flume tank one-turbine experiment [6].

of ambient turbulence can be achieved by inserting honeycomb grids with different refinements before the testing section. As reported in the schematic side view of the flume tank test section in Fig. 1, the rotor nacelle is connected to a supporting structure above the free surface by means of a hanging tower. The rotor has diameter D=0.7 m, its three blades feature the NACA 63418 and the blade chord at 80.5% rotor radius is 137 mm. The complete chord and twist profiles of the blades are provided in [6]. The cross sectional blockage, given by the ratio of rotor swept area and tank cross section, is about 4.8%. The main dimensions of the turbine and the depth of its rotational axis are reported as functions of D and H, respectively, in Fig. 1.

The test conditions considered in the present study were characterized by water speed U_∞=0.8 m/s and ambient turbulence intensity $TI_\infty = 3\%$ in the flume test section. The experiments aimed at measuring and characterizing both the turbine performance and its wake. The turbine power was provided in the form of one curve plotting the power coefficient C_P against the rotor tip-speed-ratio (TSR) λ, and one curve plotting the thrust coefficient C_T against λ. The definitions of these three parameters are:

$$\lambda = \frac{\Omega R}{U_\infty}, \quad C_P = \frac{Q\Omega}{0.5\rho A U_\infty^3}, \quad C_T = \frac{T}{0.5\rho A U_\infty^2} \quad (1)$$

where $A = \pi R^2$, ρ is the water density and Ω is the angular speed of the rotor. The TSR was varied by varying Ω, while keeping U_∞ constant. The rotor thrust T was measured by a six-component load cell in the supporting structure at the tower attachment above the free surface, and the rotor hydrodynamic torque Q was measured by a torque sensor directly fixed between the rotor and the motor. For each TSR, rotor and thrust were measured at a rate of 100 Hz for 100 seconds. Water speeds behind the turbine were measured with laser Doppler velocimetry at a rate between 6 and 33 Hz for 100 seconds. Velocity mea-

surements were taken on a matrix of points in planes behind the turbine normal to the rotor axis.

III. NUMERICAL METHOD

The main modeling and numerical methods of the CFD code used in this study are discussed in the first subsection below, whereas the physical domain, the adopted computational grid, the main parameters of the considered operating regime and the boundary conditions are reported in the second subsection.

A. Computational fluid dynamics code

All CFD simulations presented herein are carried out using version 17.2 of ANSYS FLUENT [26], an unstructured cell-centered finite volume Navier-Stokes CFD code. The simulations use the RANS flow model, and the effects of turbulence on the mean flow are accounted for by using Menter's $k - \omega$ shear stress transport (SST) turbulence model [27], a two-equation turbulence closure frequently used in TST CFD [18], [21], [28]. Some of the analyses reported in this study also use a laminar-to-turbulent transition model to account for possible blade load alterations due to transition, since the Reynolds number associated with the blade relative flow field is rather low. Herein transition is modeled by augmenting the SST model with two additional transport equations, one for the the Reynolds number based on the momentum thickness θ and one for the intermittency γ. This addition yields the four-equation $k - \omega$ SST $\gamma - Re_\theta$ transition model, whose physical and numerical details are presented in [29] and [30]. The incompressible flow equations are solved using a pressure-based solution approach. More specifically, the governing equations are solved with the FLUENT Coupled integration approach, whereby the momentum and the pressure-based continuity equations are solved in a fully-coupled fashion. The turbulence and transition model transport equations are instead integrated in a segregated or loosely coupled fashion. The space discretization of both the mean flow, turbulence and transition model equations is second order accurate, and is based on an upwind flux discretization, with the gradients of all variables being computed with a Green-Gauss cell-based approach. Calculation of the pressure on the cell faces is based on the Pressure Staggering Option (PRESTO) scheme. Further detail on the aforementioned modeling and numerical features can be found in the FLUENT theory guide [26].

B. Physical domain and boundary conditions

The selected physical domain has the same cross section of the IFREMER flume tank, and this implies that the cross sectional blockage of the experiment and the simulations is also the same, and amounts to about 4.8%. The front and side views of the physical domain are shown in the left and right images of Fig. 2, respectively. All dimensions are referred to the rotor diameter D. It is noted that the domain length upstream and downstream of the turbine is increased with respect

to the dimensions of flume tank test section to reduce the detrimental impact of spurious reflections from the far field boundaries on the computed solutions. The turbine geometry modeled in all geometry-resolved CFD analyses discussed in this paper consists of the rotor blades and the rotor nacelle, and is depicted in Fig. 3.

Fig. 2 indicates the boundary conditions (BCs) imposed at the boundaries of the considered domain. A velocity inlet BC is applied at the inlet of the numerical tank (boundary $b1$). Here, the freestream velocity U_∞, and suitable values of the freestream turbulent kinetic energy (TKE) k_∞ and the specific dissipation rate ω_∞ are prescribed. The value of k_∞ is computed using U_∞ and TI_∞ according to:

$$k_\infty = \frac{3}{2} \left(U_\infty TI_\infty \right)^2 \qquad (2)$$

The value of ω_∞ depends on both k_∞ and a turbulence integral length scale l according to:

$$\omega_\infty = \sqrt{k_\infty} / \left(C_\mu^{0.25} l \right) \qquad (3)$$

where C_μ is one of the constants of the SST model. Unless otherwise stated, the length scale l is set to the rotor radius R, consistent with the observations of [25].

A pressure outlet BC is applied at the outlet of the numerical tank (boundary $b3$), where a zero differential pressure is enforced. A viscous wall BC is used on the flume bed and lateral walls (boundaries $b4$, $b5$ and $b6$) and the surface of all three blades (boundary $b8$), whereas an inviscid wall BC is enforced at the tank free surface and rotor nacelle boundaries (boundaries $b2$ and $b7$). All the BCs applied to the boundaries of the physical domain are also listed in Table I. The use of the inviscid wall BC at the tank free surface corresponds to a rigid lid model. This choice is made to reduce the computational cost associated with use of finer grids at this location to model in a time-dependent fashion free surface dynamics. The rigid lid model is unlikely to affect rotor mean power and loads, as experimental evidence indicates a low sensitivity of these mean quantities to surface gravity waves [31]. Surface waves may affect rotor wake dynamics. However, based on the test conditions reported by IFREMER, this seems unlikely to be the case for the experiment analyzed herein. The side view of the physical domain in Fig. 2 also highlights a rectangular enclosure of the turbine, which represents the interface between a cylindrical subdomain containing the rotor and its nacelle, and the rest of the domain. As discussed in Section IV, this subdivision is needed for the time-dependent sliding mesh simulations to enable the rotor subdomain to rotate past its axis within the rest of the stationary domain.

The unstructured grid used for all rotor-resolved simulations reported in this study is made up of prisms and tetrahedra, and is generated using the ANSYS ICEM CFD grid generator. The average number of grid nodes past each blade airfoil is 160. The number of grid nodes along the blade length varies with the chordwise position, and amounts to about 1500 along both the leading and the trailing edges, and about 400

TABLE I
BOUNDARY CONDITIONS APPLIED TO PHYSICAL DOMAIN OF FIG. 2

Symbol	Quantity
$b1$	Velocity inlet
$b2, b7$	Inviscid wall
$b3$	Pressure outlet
$b4, b5, b6, b8$	Viscous wall

at 50% chord on the suction side. The inflation layer past each blade features 17 grid layers parallel to the blade surface. The height of the first grid layer above the blade surface is 4×10^{-3} mm, and this choice results in a nondimensionalized wall distance y^+ less than 1 in all CFD analyses reported below. Inflation layers are also used on flume tank bed and lateral walls. These inflation layers feature 20 layers, and the height of the first grid layer above the blade surface is 9×10^{-2} mm in all three cases. The adopted grid has a total of $35,925,000$ elements, with $28,912,170$ of these used in the rotor subdomain, and about $3,800,000$ elements in the wake region. A mesh sensitivity analysis not reported for brevity confirms that the adopted grid produced grid-independent results in terms of both turbine performance and wake resolution.

IV. RESULTS

All rotor-resolved CFD analyses presented below are performed using the computational grid presented in Section III; the results of the analysis obtained by coupling a generalized actuator disk model to the RANS equations considered in the present study are those reported in [22], and are labeled VBM, the acronym of virtual blade model; the experimental data used to validate all numerical analyses are part of those reported in [6]. Both steady and time-dependent rotor-resolved analyses are presented and discussed in the two subsections below, with the first subsection focusing on rotor performance and blade loads, and the second subsection on the resolution of the key characteristics of the rotor wake. Steady rotor-resolved simulations are carried out for $2.5 \le \lambda \le 7$, whereas a single time-dependent simulation, for the design TSR $\lambda = 3.67$, is performed and discussed. In all simulations, the conditions $U_\infty = 0.8$ m/s and $TI_\infty = 3\%$ are enforced, and λ is varied by specifying suitable values of the rotor angular speed Ω.

The steady rotor-resolved simulations use the so-called frozen-rotor approach, which amounts to solving the governing equations in the rotating, i.e. relative, frame. These analyses use FLUENT hybrid initialization, and, using the Coupled pressure-based solver, all residuals drop by four to six orders of magnitude within 5000 iterations for the fully turbulent analyses and 6500 iterations for the transitional flow analyses.

The time-dependent rotor-resolved simulation uses the so-called sliding mesh approach, whereby a cylindrical subdomain containing the turbine rotor and nacelle slides into a larger stationary domain, with flow data being exchanged at the interface of the two
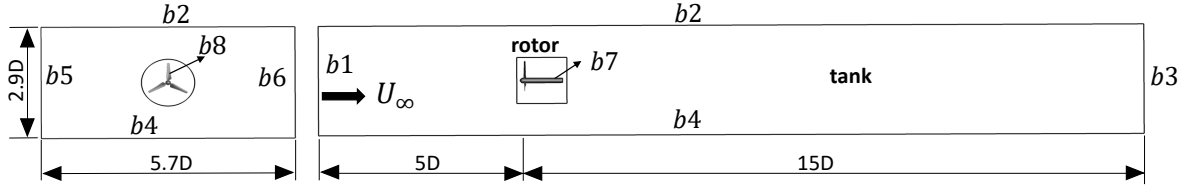
Fig. 2. Physical domain of IFREMER flume tank one-turbine experiment [6] considered in present CFD study: front view (left) and side view (right).
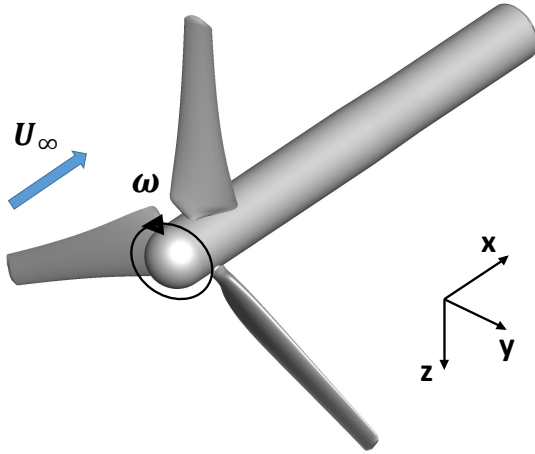

Fig. 3. Digital model of IFREMER turbine [6] adopted in present CFD study.
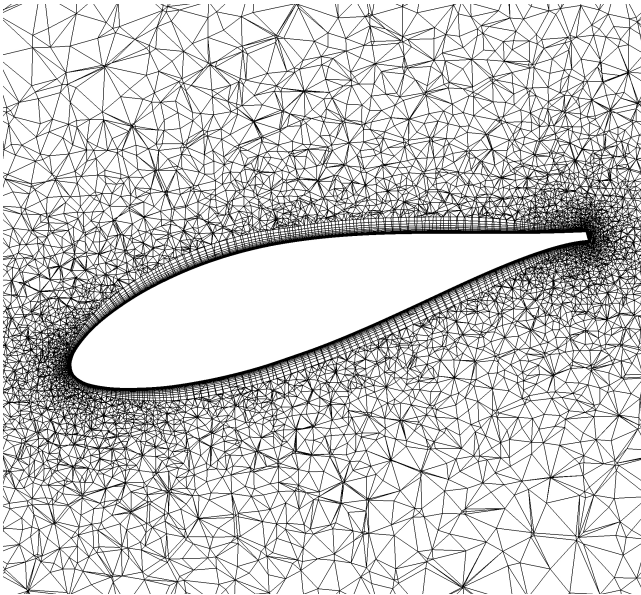

Fig. 4. Grid past blade on plane slice at 50% rotor radius.

domains at each physical time step. Using this set-up, the equations are solved in the absolute frame of reference. Twenty subiterations of the Coupled solver are carried out at each physical time-step, and this results in a reduction of all residuals of about four orders of magnitude. Each physical time-step corresponds to a

rotor angular displacement of 2°. The simulation is run for the time corresponding to 40 rotor revolutions, and the analysis of this simulation below refers to the time-averaged flow field over the last revolution.

A. Turbine performance analysis

Figure 5 compares the measured $C_P - \lambda$ curve to those computed with all tested simulation methods. The best agreement is obtained with the rotor-resolved fully turbulent analysis (curve labeled Geom. std. FT), which matches the measured data very well over the common interval of λ considered. The design value of C_P obtained with the sliding mesh rotor-resolved fully turbulent simulation (symbol labeled Geom. std. FT), differs little from its steady counterpart, indicating a negligible role of unsteady flow phenomena such as dynamic stall on the prediction of turbine performance. A similar conclusion was reported by [21]. The steady rotor-resolved analysis using the $k - \omega$ SST $\gamma - Re_\theta$ transition model to model laminar-to-turbulent transition on the turbine blades overpredicts significantly the measured C_P, which may indicate that the blade BLs in the experiment were turbulent from the leading edge (LE), despite the relatively low chord- and relative velocity-based Reynolds number Re. The mean and maximum value of this parameter are 105k and 126k, respectively. The turbine power prediction of the generalized actuator disk analysis (curve labeled VBM) is in fairly good agreement with the measured estimate in the design TSR region, but the agreement decreases as TSR increases. The lift and drag data used in the VBM analysis were obtained with the XFOIL code using Re=105k.

Figure 6 compares the measured $C_T - \lambda$ curve to those computed with all tested simulation methods. It is noted that the measured thrust includes the contribution of the tower which is instead not included in any of the numerical results, as this component is not modeled in the CFD representation. For this reason all numerical estimates of C_T are expected to be lower than the measured values. The steady rotor-resolved analysis including transition modeling predicts a higher thrust than its fully turbulent counterpart, similarly to that seen for the $C_p - \lambda$ curves. From a qualitative viewpoint, one sees that the magnitude of the difference between numerical result and measured data increases with TSR for both the VBM and the steady rotor-resolved fully turbulent analyses. This is because the rotor induction decreases as TSR
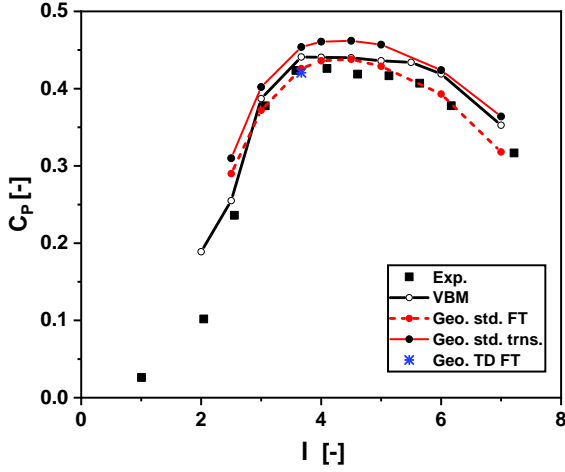
Fig. 5. Curve of power coefficient C_P against TSR λ: comparison of experimental data and results of VBM CFD analyses and rotor-resolved CFD analyses using steady fully turbulent, steady transitional and time-dependent fully turbulent flow models ($l = R$).
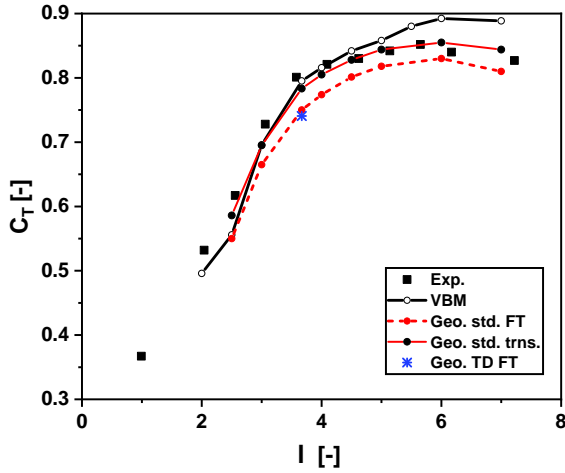

Fig. 6. Curve of thrust coefficient C_T against TSR λ: comparison of experimental data and results of VBM CFD analyses and rotor-resolved CFD analyses using steady fully turbulent, steady transitional and time-dependent fully turbulent flow models ($l = R$).

Fig. 7. Blade static pressure and viscous stress of fully turbulent and transitional flow analysis at $\lambda = 3.67$. Profiles of static pressure coefficient c_p at 18% (top left) and 95% (top right) rotor radius, and profiles of surface friction coefficient c_f at 18% (bottom left) and 95% (bottom right) rotor radius.

increases, resulting in higher axial velocity ahead of the tower and, therefore, higher thrust contribution of the tower. Use of approximate estimates of the tower thrust to correct the computed thrust curves (based on experimental correlation between Reynolds number and the mean drag coefficient of a circular section in a freestream flow), make the thrust level estimate of the rotor-resolved fully turbulent analysis closest to the measured curve of the thrust. The aforementioned correction is only qualitative, as it assumes uniform steady flow ahead of a circular cross section, ignoring both 3D flow effects at the two ends of the tower and unsteady flow effects due to the blade motion.

To visualize the impact of transition modeling on the loads acting on the blade, the blade static pressure coefficient c_p and the skin friction coefficient c_f are considered. The transitional and fully turbulent c_p and c_f profiles of the blade sections at the 18% and 95% rotor radius for $\lambda = 3.67$ are compared in the four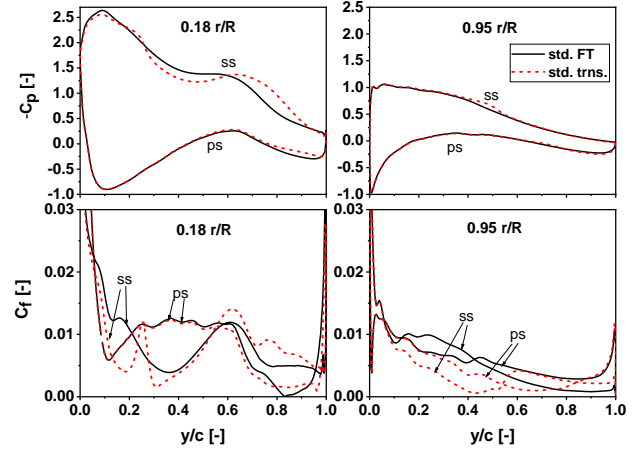 subplots of Fig. 7. At 18% radius, the flow field past the blade is highly 3D, due to finite wing effects leading to the formation of the root vortex. The c_p profile of the transitional and fully turbulent analyses present some differences in the last 20% chord of the blade pressure side (PS) (top left plot), but larger differences are observed over most of the blade suction side (SS), from about 20% chord from the LE to the trailing edge (TE). More specifically, the static pressure on the last 40% chord of the blade SS is observed to be notably smaller with the transitional flow model. As the pressure difference between the two sides of the blades at these radii is the primary force for the root vortex, this occurrence corresponds to stronger root vortices predicted by the transitional analysis. The c_f profiles of the transitional and fully turbulent analyses at the same radius also show differences on both blade sides (bottom left plot), although these differences are significantly larger on the SS. Analyzing the BL transitional state in the root region is made more complex by the significant radial flow components leading to the formation of the root vortex, but inspection of the flow field at slightly higher radii indicate that transition does not occur extensively in this region of the blade, possibly due to the low Reynolds number level at these radii ($Re \approx 50k$). At 95% rotor radius, where $Re \approx 100k$, transition is observed on both SS and PS. This is highlighted in the bottom right plot of Fig. 7, which highlights that the SS BL transition occurs starting from about 50% chord, and the PS BL transition occurs starting from about 80% chord. The effect of the SS transition is also visible in the SS c_p profile in the top right plot, which presents a slope discontinuity at 50% chord. It is observed that the key effect of transition is to increase the section loading, and, thus, rotor torque and thrust.

The profiles of tangential force F_t and normal force F_n along the blade length computed by the rotor-resolved fully turbulent and transitional analyses, and the VBM analysis at design TSR are compared in Fig. 8. The present VBM implementation does not use Prandtl tip loss correction; it rather takes the simpler
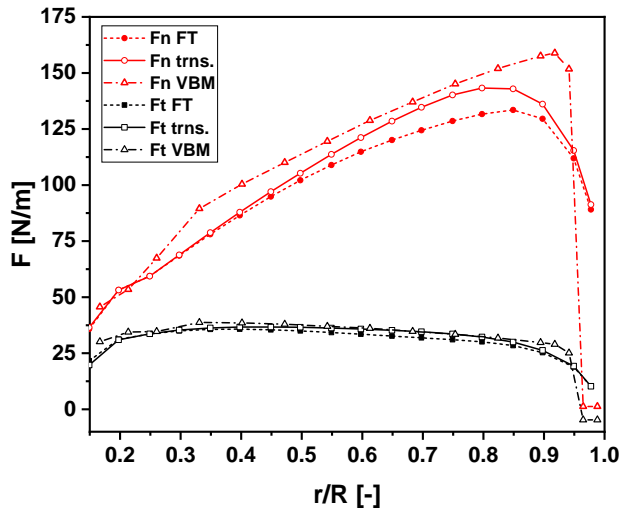
Fig. 8. Radial profiles of blade normal and tangential force computed by VBM and rotor-resolved steady fully turbulent and transitional CFD analyses.
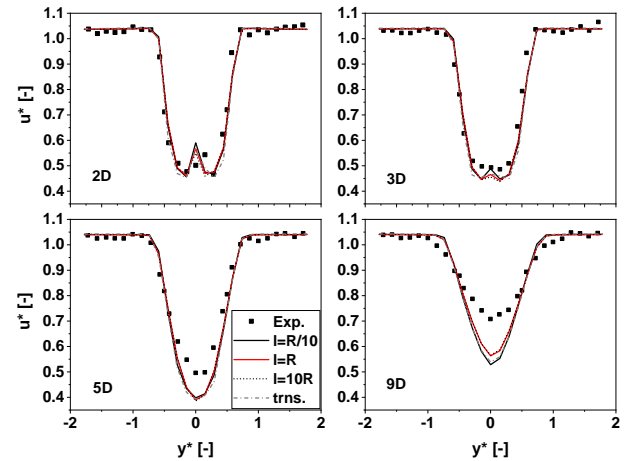

Fig. 9. Comparison of measured and computed wake velocity profiles using three values of integral scale l in fully turbulent rotor-resolved analyses, and $l = R$ in transitional flow analysis. Profiles are at 2D (top left), 3D (top right), 5D (bottom left) and 9D behind rotor.

approach of discarding all forces of the last 4% of the blade. This is the reason for the sudden drop to zero of the two VBM profiles at about 96% rotor radius. Despite this, the qualitative agreement between the rotor-resolved and the VBM profiles is very good. The force profiles of two rotor-resolved simulations are nearly superimposed for $r/R < 0.4$ and $r/R > 0.95$, a feature particularly evident for the radial profiles of F_n. Conversely, the difference between the two estimates gradually increases from 40% to about 90% rotor radius. This is because the occurrence of transition on the SS increases the blade loading, leading to higher thrust and circumferential forces. This phenomenon is the reason why the C_P curve of the transitional analysis in Fig. 5 is higher than that of the fully turbulent analysis, and the C_T curve of the transitional analysis in Fig. 6 is also higher than that of the fully turbulent analysis.

B. Wake resolution

Properly resolving the wake and correctly predicting its recovery is an important aspect of tidal turbine and array simulations. One of the input parameters that may influence the RANS predictions of turbine wake velocity deficits, turbulence levels and recovery rate is the turbulence integral length scale l appearing in Eq. (3). The turbine performance analyses discussed in the previous subsection are performed using $l = R$, and it is found that the performance of the considered turbine does not vary significantly when changing the value of this quantity, seemingly in contrast with experimental evidence [9]. The impact of this parameter on the RANS predictions of both the TKE streamwise variation in a flume tank, and the momentum extraction of porous disks modeled as uniform actuator disks placed in the tank was studied in [32], who validated their models and predictions to experimental measurements carried out in the considered facility. Here the sensitivity of the wake resolution to the value of l is assessed for the case in which a rotor-resolved

approach is used. Measured and computed profiles of the nondimensionalized flow velocity u^* behind the rotor at various downstream distances are reported in Fig. 9. The velocity u^*, which is nondimensionalized by the freestream velocity, is extracted along a horizontal line through the rotor center, and plotted against the distance y^* from the rotor center normalized by the rotor diameter D. Four frozen-rotor solutions are considered, namely the rotor-resolved fully turbulent solution for $l = R/10$, $l = R$ and $l = 10R$, and the rotor-resolved transitional solution for $l = R$. The measured profile was time-averaged, whereas the computed profiles in these figures are not circumferentially averaged. This is not done because the axial velocity field from two diameters behind the rotor is already axisymmetric. Fig. 9 shows that at downstream distances of $2D$, $3D$ and $5D$ the four numerical solutions differ negligibly from each other. At a distance of $9D$, however, the fully turbulent solution with $l = R/10$ shows a more pronounced velocity deficit than the other two fully turbulent solutions, indicating that the wake recovery rate decreases with l in the considered variability range of this parameter. Interestingly, at the distance of $9D$ the fully turbulent profile with $l = R/10$ and the transitional profile with $l = R$ present similar velocity deficits. This may be due to larger energy extraction predicted by the transitional analysis. The agreement of all predictions with measured data at $2D$ and $3D$ behind the rotor is good, whereas a growing overestimation of the velocity deficit is noted from $5D$ onward.

Fig. 10 compares the measured profiles of turbulence intensity (TI) and those predicted by the four aforementioned rotor-resolved simulations. The post-processing of the measured and computed profiles is the same adopted for the velocity profiles above, and the presented TI profiles are extracted at the same four distances from the rotor and on the same transverse lines used for the results of Fig. 9. The overall pattern and level of the four computed TI profiles differ fairly
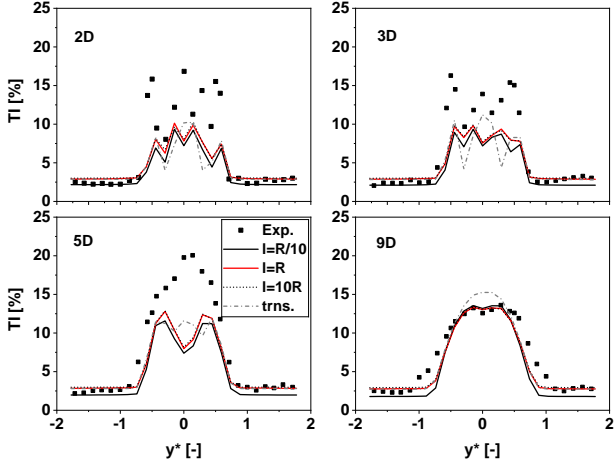
Fig. 10. Comparison of measured and computed profiles of wake turbulence intensity using three values of integral scale l in fully turbulent turbulent-resolved analyses, and $l = R$ in transitional flow analysis. Profiles are at 2D (top left), 3D (top right), 5D (bottom left) and 9D behind rotor.
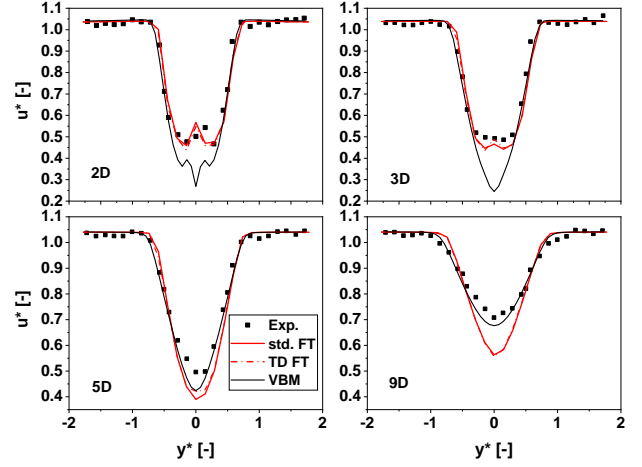

Fig. 11. Comparison of measured and computed wake velocity profiles using fully turbulent VBM, and rotor-resolved steady and time-dependent analyses ($l = R$). Profiles are at 2D (top left), 3D (top right), 5D (bottom left) and 9D behind rotor.

little at $2D$, $3D$ and $5D$ behind the rotor. In the case of the solution obtained with $l = R/10$ the ambient turbulence is reduced with respect to the value imposed at the inlet boundary, but referring the TI profile to the local ambient TI, all profiles are comparable. At $9D$, however, the $l = R/10$ and $l = R$ transitional profiles referred to the local ambient TI show a higher level of TI than the other two fully turbulent solutions. In the case of the $l = R/10$ solution this is due to the slower wake recovery when using low values of l. In the case of the transitional simulation this is due to slightly stronger root vortices, resulting in increased turbulence in the rotor hub region with respect to the case of the fully turbulent analysis. The stronger root vortices of the transitional case are due to the larger pressure difference across the rear part of the blade SS and PS near the root, as observed in Fig. 7. On the basis of the TI profiles at $2D$, $3D$ and $5D$, it appears that the overall turbulence generated by the turbine in the rotor-resolved simulations is lower than observed in the experiment.

Fig. 11 compares the measured profiles of u^* to those computed with the steady and time-dependent rotor-resolved analyses, and the VBM analysis. All three simulations use $l = R$. The four profiles of the time-dependent simulation are extracted from the flow field obtained by time-averaging the time-dependent flow field over the last simulated revolution of the simulation. One observation is that the steady and time-averaged CFD profiles are very close to each other, indicating small flow nonlinearity already at $2D$ behind the rotor. At two and three diameters behind the turbine, the rotor-resolved predictions of the wake velocity deficit are in very good agreement with measured data whereas the actuator disk analysis overpredicts the velocity deficit. At $5D$, however, there is a trend inversion, and the actuator disk solution matches more closely the experimentally observed wake recovery, whereas the rotor resolved simulations seem to dissipate the wake too slowly, surprisingly. These

phenomena are partly explained by the TI profiles of the same solutions and the experiment discussed below.

Fig. 12 compares the measured TI profiles to those computed with the steady and time-dependent rotor-resolved analyses, and the VBM analysis. All three simulations use $l = R$. As for the case of the velocity profiles, the steady and the time-averaged profiles of the sliding mesh solutions are very close to each other. The VBM predictions of the TI profiles match their measured counterparts quite well at all four axial positions, whereas the rotor-resolved analyses underpredict the TI level of the wake at $2D$, $3D$ and $5D$ behind the rotor. The VBM simulation appears to generate more turbulence behind the rotor, at a level closer to that observed in the experiment. The actuator disk analysis also correctly predicts the sharp reduction of TKE between $5D$ and $9D$. At $9D$, both rotor resolved and actuator disk profiles appear to be in good agreement with the measurements, although the TI variation rate from the rotor to $9D$ predicted by the two simulation types are substantially different. The overall patterns of the u^* and TI profiles of the VBM and rotor-resolved analyses at the considered axial stations show that the rotor-resolved simulation predicts more reliably the wake velocity deficit within a short distance of the rotor but the velocity deficit recovery is slower than observed in the measurements and predicted by the VBM analysis. This is because the rotor-resolved analysis generates less turbulence behind the rotor than observed in the measurements and predicted by the VBM analysis: a faster wake recovery is prevented by both the lower turbulence behind the rotor and the low level of ambient turbulence of this test. However, in contrast with the rotor-resolved analysis, the VBM analysis overpredicts the velocity deficit close to the rotor, but accomplishes a good prediction of the velocity deficit sufficiently far downstream, due to relatively fast wake recovery enabled by higher turbulence in the wake. Qualitatively, these trends are in line with those observed in other AD-based RANS studies of
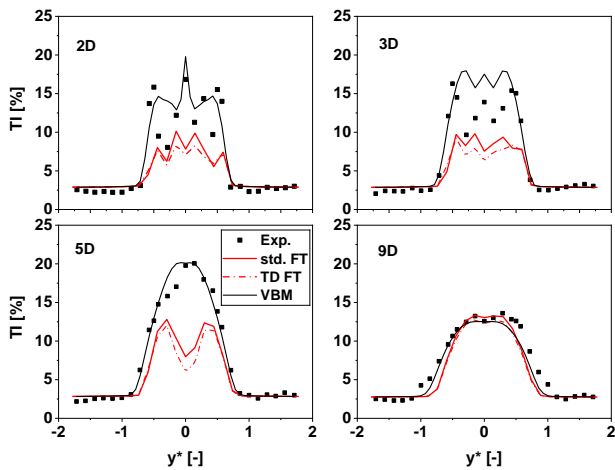
Fig. 12. Comparison of measured and computed profiles of wake turbulence intensity using fully turbulent VBM, and rotor-resolved steady and time-dependent analyses ($l = R$). Profiles are at 2D (top left), 3D (top right), 5D (bottom left) and 9D behind rotor.

TSTs, although improvements of the blade tip loss model of the BEMT model embedded in the RANS simulation, have been shown to significantly improve the agreement of computed and measured wake data for this test case [33].

The left and right images of Fig. 13 depict the blade tip vortices predicted by the steady frozen rotor and time-dependent simulations, respectively. The isosurface of the Q-criterion [34] at 0.5 s^{-2} is used in both cases, and the time-dependent result is the snapshot corresponding to the rotor having the same angular position as that of the steady frozen rotor analysis. One sees that the time-dependent analysis resolves the blade tip vortices for a longer axial distance than the frozen rotor analysis, since this latter cuts all vortices at about one diameter behind the rotor, at the downstream interface of the relative and absolute subdomains. This occurrence points to the fact that it is advisable to place the aforementioned interface as far downstream as possible when using the frozen rotor approach and not including the rotor support structure in the simulation. The fairly small solution discontinuities at the same interface observed in the time-dependent solution also highlight the importance of adopting a high grid refinement across the interface between the relative and absolute domains, since these discontinuities originate from unavoidable solution interpolation errors at this interface. Finally, it is noted that despite these differences in the resolution of the tip vortices, the steady solution and the time-dependent solution averaged over one period of revolution are extremely close, as highlighted by the results of Figures 11 and 12.

V. CONCLUSIONS

The study has presented a comparative analysis of the predictive capabilities of two RANS approaches for TST performance and wake analysis, one resolving the bladed rotor geometry, and the other replacing the turbine geometry with a generalized actuator disk (VBM approach). All computed results have been assessed against preexisting measured data of a model turbine flume tank experiment at an ambient TI of 3%. It has been found that the rotor-resolved method provides very good predictions of the turbine performance over the entire range of TSR considered. The turbine performance prediction of the VBM approach presents some more deviations from measured data, but good overall agreement of the blade loads predicted by both CFD approaches is observed. Cross-comparative analyses of the turbine performance measured in the flume tank and computed using fully turbulent and transitional flow analyses appear to indicate that the blade BLs in the experiment were fully turbulent, despite the low ambient TI level.

The rotor-resolved method provides very good predictions of the wake velocity deficit up to about $4D$ downstream of the considered turbine, and the VBM analysis provided a better match of the measured velocity profiles only after this position. The VBM analysis of this study predicts more turbulence behind the rotor than the rotor-resolved analysis, yielding a wake recovery rate closer to the measured value between $5D$ and $9D$. A sensitivity analysis on the dependence of the wake characteristics of the resolved rotor on the turbulence integral scale used as a boundary condition at the inlet boundary, led to conclusions similar to those observed for the actuator disk in previous studies, that the optimal value of this parameter is about one rotor radius. The time-averaged results of a time-dependent sliding mesh analysis at design TSR have been found to differ negligibly from the their frozen-rotor counterparts in terms of both rotor performance and wake characteristics.

The predictions of the the actuator disk method of this study may be achieved also by improving the tip flow model, as this affects the shear level between the wake and the surrounding flow. The use of Navier-Stokes CFD to predict turbine performance, wake velocity deficits and recovery rates, and losses due to wake/turbine interaction in real arrays, characterized by high and highly anisotropic turbulence, however, will require using and improving more sophisticated numerical approaches to flow turbulence, such as hybrid RANS/LES.

REFERENCES

[1] IRENA, *Renewable Power Generation Costs in 2019.* Abu Dhabi: Earthscan, 2019.

[2] P. Robins, S. Neill, and M. Lewis, "Impact of tidal-stream arrays in relation to the natural variability of sedimentary processes," *Renewable Energy*, vol. 2, pp. 311–321, 2014.

[3] C. Vogel, D. Taira, B. Carmo, G. Assi, R. Willden, and J. Meneghini, "Prospects for Tidal Stream Energy in the UK and South America: A Review of Challenges and Opportunities," *Polytechnica*, vol. 2, p. 97–109, 2019.

[4] A. Roberts, B. Thomas, P. Sewell, Z. Khan, S. Balmain, and J. Gillman, "Current tidal power technologies and their suitability for applications in coastal and marine areas," *Journal of Ocean Engineering and Marine Energy*, vol. 2, p. 227–245, 2016.
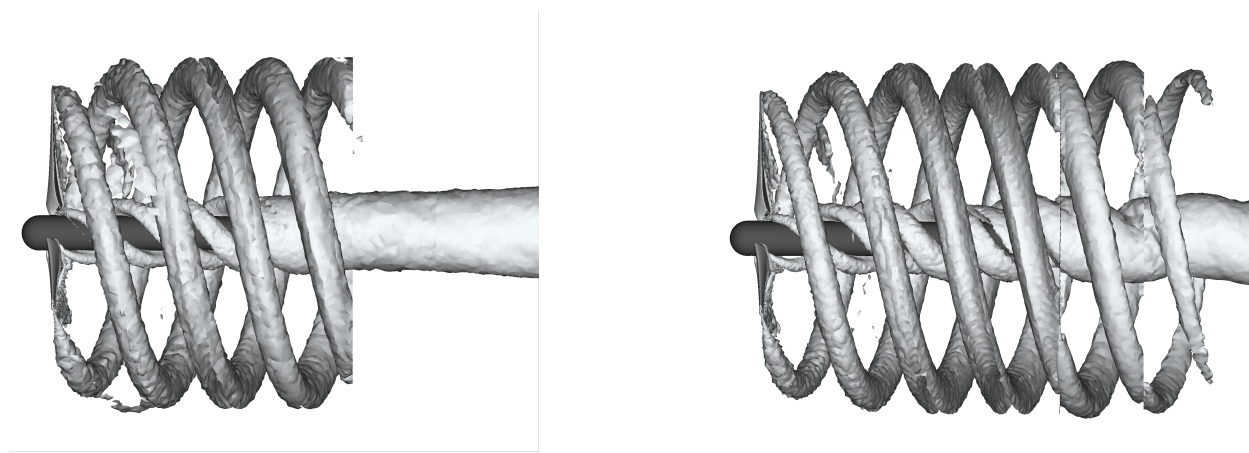
Fig. 13. Visualization of blade tip vortices using isosurface of Q-criterion of 0.5 s^{-2}: steady frozen rotor solution (left) and snapshot of time-dependent sliding mesh solution (right).

[5] R. Vennell, S. W. Funke, S. Draper, C. Stevens, and T. Divett, "Designing large arrays of tidal turbines: A synthesis and review," *Renewable and Sustainable Energy Reviews*, vol. 41, pp. 454–472, 2015.

[6] P. Mycek, B. Gaurier, G. Germain, G. Pinon, and E. Rivoalen, "Experimental study of the turbulence intensity effects on marine current turbines behaviour. part i: One single turbine," *Renewable Energy*, vol. 66, pp. 729–746, 2014.

[7] ——, "Experimental study of the turbulence intensity effects on marine current turbines behaviour. part ii: Two interacting turbines," *Renewable Energy*, vol. 68, pp. 876–892, 2014.

[8] S. Tedds, I. Owen, and R. Poole, "Near-wake characteristics of a model horizontal axis tidal stream turbine," *Renewable Energy*, vol. 63, pp. 222–235, 2014.

[9] T. Blackmore, L. E. Myers, and A. S. Bahaj, "Effects of turbulence on tidal turbines: Implications to performance, blade loads, and condition monitoring," *International Journal of Marine Energy*, vol. 14, pp. 1–26, 2016.

[10] I. Afgan, J. McNaughton, S. Rolfo, D. Apsley, T. Stallard, and P. Stansby, "Turbulent flow and loading on a tidal stream turbine by les and rans," *International Journal of Heat and Fluid Flow*, vol. 43, pp. 96–108, 2013.

[11] P. Spalart, W.-H. Jou, M. Strelets, and S. Allmaras, "Comments on the Feasibility of LES for Wings, and on a Hybrid RANS/LES approach," Proceeding of the First AFOSR International Conference on DNS/LES, August 1997, advances in DNS/LES, Ruston, Louisiana.

[12] P. Spalart, S. Deck, M. Shur, K. Squires, M. Strelets, and A. Travin, "A New Version of Detached-eddy Simulation, Resistant to Ambiguous Grid Densities," *Theoretical Computational Fluid Dynamics*, vol. 20, pp. 181–195, June 2006.

[13] Y. Chen, B. Lin, J. Lin, and S. Wang, "Experimental study of wake structure behind a horizontal axis tidal stream turbine," *Applied Energy*, vol. 196, pp. 82–96, 2017.

[14] W. Hunter, T. Nishino, and R. H. Willden, "Investigation of tidal turbine array tuning using 3D Reynolds-Averaged Navier–Stokes simulations," *International Journal of Marine Energy*, vol. 10, pp. 39–51, 2015.

[15] R. Malki, I. Masters, A. J. Williams, and T. Nick Croft, "Planning tidal stream turbine array layouts using a coupled blade element momentum – computational fluid dynamics model," *Renewable Energy*, vol. 63, pp. 46–54, 2014.

[16] J. Sørensen and W. Shen, "Numerical Modeling of Wind Turbine Wakes," *Journal of Fluids Engineering*, vol. 214, no. 2, pp. 393–399, 2002.

[17] G. Deskos, "Wake predictions from two turbine models using mesh-optimisation techniques," in *Proceedings of the Twelfth European Wave and Tidal Energy Conference*, A. Lewis, Ed. University College Cork, Ireland: EWTEC, Aug 27–Sep 1 2017, pp. 668-1–668-10, ISSN: 2309-1983.

[18] D. Apsley, T. Stallard, and P. Stansby, "Actuator-line cfd modelling of tidal-stream turbines in arrays," *Journal of Ocean Engineering and Marine Energy*, vol. 4, pp. 259—271, 2018.

[19] G. Amato, S. Doyle, S. Petley, M. Campobasso, I. Milne, and G. Aggidis, "Navier-stokes cfd analysis of a tidal turbine rotor in steady and planar oscillatory flow," in *Proceedings of the Twelfth European Wave and Tidal Energy Conference*, A. Lewis, Ed. University College Cork, Ireland: EWTEC, Aug 27–Sep 1 2017, pp. 868-1–868-10, ISSN: 2309-1983.

[20] S. Tatum, C. Frost, M. Allmark, D. O'Doherty, A. Mason-Jones, P. Prickett, R. Grosvenor, C. Byrne, and T. O'Doherty, "Wave–current interaction effects on tidal stream turbine performance and loading characteristics," *International Journal of Marine Energy*, vol. 14, pp. 161–179, 2016.

[21] T. Leroux, N. Osbourne, and D. Groulx, "Numerical study into horizontal tidal turbine wake velocity deficit: Quasi-steady state and transient approaches," *Ocean Engineering*, vol. 181, pp. 240–251, 2019.

[22] F. Attene, F. Balduzzi, A. Bianchini, and M. S. Campobasso, "Using experimentally validated navier-stokes cfd to minimize tidal stream turbine power losses due to wake/turbine interactions," *Sustainability*, vol. 12, no. 21, 2020.

[23] M. Nuernberg and L. Tao, "Experimental study of wake characteristics in tidal turbine arrays," *Renewable Energy*, vol. 127, pp. 168–181, 2018.

[24] T. Ebdon, D. O'Doherty, T. O'Doherty, and A. Mason-Jones, "Modelling the effect of turbulence length scale on tidal turbine wakes using advanced turbulence models," in *Proceedings of the Twelfth European Wave and Tidal Energy Conference*, A. Lewis, Ed. University College Cork, Ireland: EWTEC, Aug 27–Sep 1 2017, pp. 906-1–906-10, ISSN: 2309-1983.

[25] T. Ebdon, M. J. Allmark, D. M. O'Doherty, A. Mason-Jones, T. O'Doherty, G. Germain, and B. Gaurier, "The impact of turbulence and turbine operating condition on the wakes of tidal turbines," *Renewable Energy*, vol. 165, pp. 96–116, 2021.

[26] Ansys-Inc, "Fluent theory guide, release 17.2," 2016.

[27] F. Menter, "Two-equation Turbulence-models for Engineering Applications," *AIAA Journal*, vol. 32, no. 8, pp. 1598–1605, August 1994.

[28] C. Liu and C. Hu, "An actuator line - immersed boundary method for simulation of multiple tidal turbines," *Renewable Energy*, vol. 136, pp. 473–490, 2019.

[29] R. Langtry, F. Menter, , S. Likki, Y. Suzen, P. Huang, and S. Völker, "A Correlation-Based Transition Model Using Local Variables — Part II: Test Cases and Industrial Applications," *Journal of Turbomachinery*, vol. 128, no. 3, pp. 423–434, July 2006.

[30] R. Langtry and F. Menter, "Correlation-Based Transition Modeling for Unstructured Parallelized Computational Fluid Dynamics Codes," *AIAA Journal*, vol. 47, no. 12, p. 2894–2906, December 2009.

[31] E. E. Lust, L. Luznik, K. A. Flack, J. M. Walker, and M. C. Van Benthem, "The influence of surface gravity waves on marine current turbine performance," *International Journal of Marine Energy*, vol. 3-4, pp. 27–40, 2013, special Issue – Selected Papers - EWTEC2013.

[32] T. Blackmore, W. Baten, M. Harrison, and A. Bahaj, "The sensitivity of actuator-disc rans simulations to turbulence length scale assumptions," in *European Wave and Tidal Energy Conference*, Southampton, UK, September 2011.

[33] M. Edmunds, A. Williams, I. Masters, and T. Croft, "An enhanced disk averaged cfd model for the simulation of horizontal axis tidal turbines," *Renewable Energy*, vol. 101, pp. 67–81, 2017.

[34] Z. Carr, C. Chen, and M. Ringuette, "Finite-span rotating wings: three-dimensional vortex formation and variations with aspect ratio," *Experiments in Fluids*, vol. 54, pp. 1–26, 2013.